이학석사 학위논문

PET and fluorescence imaging of translocator protein 18 kDa expression in rodent models of myocarditis and glioblastoma

심근염 및 교모세포종 모델에서 PET과 형광영상을 이용한 전이체 단백질 18 kDa 발현의 평가

2018년 2월

서울대학교 융합과학기술대학원

융합과학부 방사선융합의생명전공

김 가 람

PET and fluorescence imaging of translocator protein 18 kDa expression in rodent models of myocarditis and glioblastoma

지도교수 김 상 은

이 논문을 이학석사 학위논문으로 제출함

2018년 1월

서울대학교 융합과학기술대학원

융합과학부 방사선융합의생명전공

김 가 람

김가람의 이학석사 학위논문을 인준함

2018년 1월

위 원 장 박 원 철 (인)

부위원장 김 상 은 (인)

위 원 이 원 우 (인)

Abstract

PET and fluorescence imaging of translocator protein 18 kDa expression in rodent models of myocarditis and glioblastoma

Ga Ram Kim

Program in Biomedical Radiation Sciences

Graduate School of Convergence Science and Technology

Seoul National University

Translocator protein 18 kDa (TSPO), which is located mainly in the outer membrane of the mitochondria, is considered as a potential biomarker of inflammation or specific cancers because of its overexpression in such lesions. This protein is closely associated with inflammatory responses in various diseases, including myocarditis or glioblastoma multiforme (GBM). Here, we evaluated TSPO overexpression using TSPO radiotracers, [^{18}F]fluoromethyl-PBR28 ([^{18}F]**1**) and [^{18}F]CB251 ([^{18}F]**2**), and TSPO-targeted iron oxide nanoparticles in different rodent disease models to precisely diagnose each lesion. Both the radiotracers, [^{18}F]**1** and [^{18}F]**2**, were successfully prepared in an automated module and compared between in an experimental autoimmune

myocarditis (EAM) model and a healthy control by positron emission tomography (PET) imaging to determine which is more suitable for *in vivo* TSPO assessment. [^{18}F]**2** showed a more specific TSPO uptake in the heart of EAM rats (1.32-fold higher heart-to-lung uptake ratio) than in that of healthy rats, whereas [^{18}F]**1** showed similar heart uptake patterns between the two groups. Histopathological analysis of the heart tissues from each group demonstrated abnormal TSPO expression in inflammatory myocardial tissues compared with control tissues. Nanoparticles were prepared with TSPO ligands (CB235) and Cy5.5 dyes which were introduced on the surface of the nanoparticles, and were evaluated in a subcutaneously implanted glioblastoma xenograft mouse model by fluorescence imaging. The fluorescence signal from tumors was strongest at 8 h, and 71.3% of the uptake at 8 h was maintained after 24 h despite rapid clearance from other organs (highest tumor-to-background ratio at 24 h). These results demonstrated that the imidazole[1,2-a]pyridine-based radiotracer [^{18}F]**2** is a sensitive tool for the noninvasive diagnosis of myocarditis; thus, it may be applied to clinical settings for the early diagnosis of human myocarditis. Moreover, the tumors were visualized using TSPO-targeted fluorescent nanoparticles. The findings suggest that the specificity and selectivity of TSPO-targeted nanoparticles may facilitate tumor diagnosis, serving as a guide for surgical treatment.

Keywords: translocator protein, myocarditis, glioblastoma multiforme, positron emission tomography, fluorescence imaging

Student number: 2016-26046

CONTENTS

LIST OF TABLES

LIST OF FIGURES

INTRODUCTION

1. Translocator protein 18 kDa (TSPO)

Translocator protein 18 kDa (TSPO), which is located mainly in the outer membrane of the mitochondria, is a well-established biomarker of brain injury or cancer because it is overexpressed in such lesions [1-3]. Originally, TSPO was identified as a peripheral benzodiazepine receptor (PBR); however, this definition was changed following subcellular functional studies [1,4]. TSPO regulates cholesterol transport, cell proliferation, apoptosis, and inflammation [4-6]. Particularly, TSPO has a close relationship with inflammatory responses under pathological conditions. Therefore, it is useful to employ TSPO-selective ligands as radiotracers or nanoparticles to detect *in vivo* inflammation with macrophage infiltration. Nevertheless, studies have been limited to specific diseases such as glioblastoma, neurodegeneration, and prostate or breast cancer [7-9]. These studies are actively performed as TSPO expression is abnormally increased in the Schwann cells, macrophages and neurons of the peripheral nervous system [2]. Recently, several studies have been conducted using TSPO as a diagnostic tool in various pathological conditions including myocardial inflammation as TSPO was found to be overexpressed in myocardial inflammatory foci [10,11].

2. PET and radiotracers for diagnosing myocarditis

Positron emission tomography (PET) is a nuclear imaging technique that provides information on functional mechanisms in the human body. PET is based on the physical properties of isotopes emitting positrons when they decay. Radionuclides decay in the body on a biologically active molecule with the release of a positron known as a β-particle. This β-particle travels a short distance and is annihilated with an anti-particle. Annihilation results in the formation of two high-energy photons (511 keV each) that travel in opposite directions, which can be detected by two diametric detectors. The radionuclides for PET imaging are typically isotopes with short half-lives such as ^{11}C, ^{13}N, ^{15}O, and ^{18}F. Since PET imaging sheds light on biochemical functions in the body, it has been extensively used to diagnose diseases [12].

Myocarditis is an inflammation of the heart muscle. This disease has a relatively low incidence but is extremely difficult to diagnose accurately at an early stage because the symptoms, such as chest pain, myocardial dysfunction, and even dyspnea, can be similar to those of other heart diseases such as myocardial infarction [13-15]. The clinical variations of myocarditis are associated with those ambiguous symptoms. Furthermore, myocarditis is pervasive and can be fatal in children and seniors with weakened immune systems [16-18]. Therefore, myocarditis should be diagnosed at an early stage. Biopsy is the gold standard for accurate diagnosis; however, it is highly invasive and thus not as widely used as non-invasive diagnosis [19,20]. Cardiac magnetic resonance imaging (cMRI) and echocardiography (ECG) are

conventional imaging methods for detecting myocarditis but have limited sensitivity and specificity [21,22]. In contrast, nuclear imaging can be used to acquire functional images with high sensitivity for heart diseases such as myocardial infarction, myocarditis, and cardiomyopathy [23,24]. By using an appropriate radiotracer to target inflammatory lesions, the efficiency of myocarditis detection can be maximized. Hence, we used TSPO-specific radiotracers and PET imaging for early diagnosis.

Here, we describe the *in vivo* evaluation of two classes of TSPO-selective PET radiotracers for detecting myocardial inflammatory foci by assessing TSPO expression in a rat model of experimental autoimmune myocarditis (EAM) (Figure 1). [^{18}F]Fluoromethyl-PBR28 ([^{18}F]**1**, IC_{50} = 8.28 nM) is an aryloxyanalide analogue and a promising *in vivo* TSPO biomarker of neuroinflammation [25]. Another TSPO radiotracer, [^{18}F]CB251 ([^{18}F]**2**, K_1 = 0.27 nM), is a slightly modified compound derived from alpidem in the imidazopyridine acetamide class [9,26]. In a previous study, [^{18}F]**2** was used to detect neuroinflammation and TSPO-rich cancer in mouse models as a favorable imaging probe with specific uptake in lesions. Many researchers have evaluated myocardial inflammation using TSPO-selective radiotracers in recent years. [^{125}I]IodoDPA-713 is a typical probe used for evaluation in mouse models of coxsackievirus B3 (CVB3) myocarditis [27,28]. However, the direct and effective diagnosis of myocarditis is limited by low heart uptake, high lung uptake, etc. Therefore, we used two different classes of TSPO radiotracers to specifically detect myocardial inflammation at an early stage.

3. Fluorescent visualization of glioblastoma

Glioblastoma multiforme (GBM) is the most lethal type of human brain cancer, and an average of 60% of patients with brain cancer have glioblastoma [29]. Generally, the median survival time for patients with this disease is 15–16 months with surgery or therapy; however, survival time varies depending on the patients and their health [30,31]. The greatest challenge in glioblastoma is diagnosis and prognosis because of its rapid growth rate and limitations in early checkup. If specific signs are observed during neurological examination by specialists, imaging diagnosis is required [31,32]. Typically, magnetic resonance imaging (MRI), computerized tomography (CT), and PET are performed to diagnose the grade and metastasis of brain tumors [33,34]. Nevertheless, biopsy remains as the gold standard for the final diagnosis of glioblastoma even though this methodology has a critical limitation, which is invasiveness [35]. In addition, determining the tumor capacity and margin for surgical treatment is extremely difficult under operative conditions [36,37]. Therefore, if the direct and accurate diagnosis of tumor margins using fluorescence imaging techniques, which are more sensitive than conventional imaging modalities, is possible as a pre-operative guidance without biopsy, it may improve surgical or therapeutic planning and minimize remaining margins and side effects.

In the medical field, fluorescence imaging has been used as a guided imaging technique to identify tumors and metastases because of its high sensitivity and flexibility [38,39]. The near–infrared (NIR) region, which ranges from 700 nm to 900 nm, is widely used for *in vivo* fluorescence imaging

because of deep tissue penetration and minimal autofluorescence [40,41]. Owing to these intrinsic characteristics, fluorescent dye-labeled iron oxide nanoparticles can be used for tumor visualization. This nanoparticle has great advantages in terms of surface modification, blood circulation and target specificity [42-44]. Therefore, it will be possible to detect specific tumor areas if the overexpressed TSPO in the tumor is bound to TSPO-selective nanoparticles with NIR fluorescent dyes.

In this study, we evaluated TSPO expression in an U87-MG (human glioblastoma cell) xenograft mouse model using TSPO-targeted fluorescent nanoparticles. CB235, a TSPO-selective ligand, and cyanine 5.5 (Cy5.5), a NIR fluorescent dye, were introduced on the surface of iron oxide nanoparticles. CB235 is a TSPO ligand in the imidazopyridine acetamide class. It is similar to CB251 but is more suitable than CB251 for attachment to iron oxide nanoparticles. Based on the structure of the nanoparticle, the tumor may be visualized with both active targeting from TSPO-targeted ligands and passive targeting from the well-known enhanced permeability and retention (EPR) effect of nanoparticles.

4. Research objectives

A. We assessed TSPO overexpression in an EAM rat model (a non-tumor model) and a subcutaneously implanted glioblastoma xenograft mouse model (a typical tumor model) using TSPO-selective radiotracers or nanoparticles.

B. We specifically visualized the inflammatory foci and tumor area closely associated with TSPO overexpression using PET or optical imaging techniques.

C. We used TSPO-targeted ligands, which are a promising diagnostic tool in various medical fields.

MATERIALS AND METHODS

1. Assessment of TSPO in myocarditis by PET imaging

Synthesis of radiotracers

[^{18}F]Fluoride was produced at Seoul National University Bundang Hospital using proton bombardment of an ^{18}O-enriched water target in the KOTRON-13 cyclotron (Samyoung Unitech Co., Seoul, Korea). ^{18}F was isolated from the enriched water by trapping in a Chromafix-HCO_3 cartridge previously activated with 2 mL of ethanol and 5 mL of water. After azeotropic distillation of a mixture of acetonitrile (CH_3CN) and water (1:0.2 mL) dissolved $K_{2.2.2}/K_2CO_3$ (15 mg/2.7 mg) by helping additional CH_3CN (0.3 mL) and a nitrogen stream, a solution of dibromomethane (50 μg) in acetonitrile (1 mL) was subsequently added and mixture was heated at 120°C for 5 min. The synthesis of [^{18}F]**1** was performed in the TRACERlab FX N pro (GE Healthcare, Little Chalfont, UK) and consisted with two reactors. The obtained CH_2Br[^{18}F]F was distilled into a precooled second reactor (-10°C), containing desmethyl-PBR28 (1 mg) and 5 N NaOH (6 μL) in *N*,*N*-dimethylformamide (DMF, 0.7 mL). The distillation of CH_2Br[^{18}F]F was carried out under 75 mL/min helium flow through in series of four C18 environmental Sep-Pak cartridges. When radioactivity reached a peak, the solution was heated at 100°C for 5 min. After cooling to approximately 40°C, the reaction mixture was diluted with 10 mL of water. This solution was loaded into a tC18 Sep-Pak cartridge (Waters,

Milford, MA, USA), washed with 10 mL of water, and eluted with 1.5 mL of CH_3CN. After dilution with 1.5 mL of water, the combined solution was separated by a semi-preparative HPLC system (Xterra RP18, 10 × 250 mm, 45% CH_3CN/water, flow rate: 3 mL/min) using a UV detector at 254 nm and gamma-ray detector (Bioscan, Poway, CA, USA). The product fraction was collected after approximately 13.5 min and the fraction of [^{18}F]**1** collected from the HPLC system was diluted with 20 mL of water. The diluted solution was exchanged to 8% ethanol (EtOH)/saline solution by a tC18 Sep-Pak cartridge for further biological evaluation. The second TSPO radiotracer, [^{18}F]**2**, was prepared by nucleophilic aliphatic substitution on a tosylate precursor with fluorine-18 in a single-step radiolabeling procedure as previously described with slight modification [45]. The synthesis was performed in the TRACERlab FX_{FN} (GE Healthcare). Briefly, the trapped fluorine-18 in a Chromafix-HCO_3 cartridge eluted with a mixture of methanol and water (1:0.1 mL) was dissolved with 40% tetrabutylammonium bicarbonate (10 µL). The eluted solution containing fluorine-18 was dried by azeotropic distillation under a nitrogen stream and subsequently mix with a tosylate precursor (3.0 mg) in *tert*-amylacohol:DMF (v/v, 9:1, 1 mL). The reaction mixture was heated to 120°C for 10 min and cooled to approximately 40°C. The diluted solution with 10 mL of water was loaded into a C18 plus Sep-Pak cartridge (Waters), washed with 10 mL of water, and eluted with 1.5 mL of CH_3CN. After dilution with 1.5 mL of water, the combined solution was isolated by a semi-preparative HPLC system (Xterra RP18, 10 × 250 mm, 55%

CH_3CN/water, flow rate: 4 mL/min) using a UV detector (254 nm) and gamma-ray detector. The product fraction was acquired after approximately 17 min and the fraction of [^{18}F]**2** was diluted with 20 mL of water. This solution was exchanged to 8% EtOH/saline solution by a C18 plus Sep-Pak cartridge for further biological evaluation.

Metabolite testing

Blood and hearts were collected 60 min after the intravenous injection of [^{18}F]**2** from male Balb/c mice (7 weeks old, n = 12). Blood was obtained and centrifuged at 15,000 rpm for 1 min. The plasma (0.5 mL) was separated and transferred to a tube containing acetonitrile (0.5 mL). The mixture was stirred in a vortex mixer and centrifuged at 15,000 rpm for 2 min to separate the precipitate from the aqueous phase. The heart was placed in test tubes (each containing 2.5 mL of cold saline) and homogenized (SilentCrusher-S; Heidolph Instruments, Schwabach, Germany). The heart tissue homogenate (0.5 mL) was transferred to a tube containing acetonitrile (0.5 mL) and centrifuged at 15,000 rpm for 2 min. The precipitate and supernatant were separated and measured for radioactivity. The supernatants of the plasma and heart homogenates were analyzed using a HPLC system equipped with a highly sensitive detector for radioactivity. The HPLC system and conditions were as follows: pump, PU-2089 Plus (Jasco, Oklahoma City, OK, USA); ultraviolet detector, UV-

2075 (Jasco); NaI(Tl) scintillation detector, S-2493A (OKEN, Tokyo, Japan); pre-column, XBridge Prep C18 Guard Cartridge (5 mm, 10 mm i.d. · 10 mm; Waters); main column, XBridge OST C18 (2.5 mm, 10 mm i.d. · 50 mm; Waters); mobile phase, 90% aqueous acetonitrile/0.02 M sodium phosphate buffer (pH 7.0) (30/70 [0–4 min], 40/60 to 70/30 [4–7 min], v/v); flow rate, 8.0 mL/min; and tR, [^{18}F]**2**, 12.5 min. All procedures in this section were performed with the fluorescent light switched off.

Animal models

Male Lewis rats (7 weeks old) weighing 200–250 g were purchased from Orient Biotech (Seoul, Korea), and EAM rats were prepared as previously reported [46]. Before the experiment, the rats were stabilized for 1 week. The rats were immunized with purified porcine cardiac myosin (troponin I peptide; Sigma, St. Louis, MO, USA) suspended in an equal volume of complete Freund's adjuvant (Sigma). This mixture was injected into the footpad once a week. After 3 weeks of immunization, microPET imaging was performed using EAM rats and healthy control rats (n = 5, respectively). All animals were monitored and fed a regular diet. All animal experiments in this study were approved by the Seoul National University Bundang Hospital Animal Care and Use Committee (BA1408-158/038-02) and conformed to NIH guidelines (Guide for the Care and Use of Laboratory Animals).

microPET imaging

Rats were anesthetized with 2% isoflurane in oxygen gas and intravenously injected with saline containing 22.5–25.9 MBq of TSPO radiotracers ([^{18}F]**1** or [^{18}F]**2**) via the lateral caudal vein (Figure 3A). After radiotracer injection, PET images were acquired for 60 min in list mode using NanoScan® PET/CT (Mediso Ltd., Budapest, Hungary). For blocking analysis, which was performed to determine the *in vivo* specificity of heart uptake in EAM rats (n = 3), additional PET images of [^{18}F]**2** were obtained following the same protocol after treatment with PK11195 (10 mg/kg) 10 min before injecting [^{18}F]**2**.

PET image analysis

Analysis of PET images was performed using AMIDE software. A region of interest (ROI) was drawn for both the whole myocardium and lung. The heart-to-lung uptake ratio (HLR) was semi-quantified using the ROI in TSPO imaging with each radiotracer [47].

Western blot analysis

Western blotting was performed using standard methodology [48]. After PET imaging, the rats were sacrificed. Heart tissues were isolated for protein extraction. The proteins from each sample were separated by

electrophoresis and electrotransferred to polyvinylidene fluoride membranes. The membranes were immunoblotted with rabbit monoclonal PBR antibody (1:10000; Novus Biologicals, Littleton, CO, USA) followed by goat anti-rabbit IgG-HRP (1:5000; Santa Cruz Biotechnology, Dallas, TX, USA). The proteins were detected by chemiluminescence assay (Pierce™ Fast Western Blot Kit; Thermo Fisher Scientific, Waltham, MA, USA). The relative band density was analyzed using ImageJ (open source image processing software).

Immunohistochemistry

Heart samples were isolated and fixed with 4% paraformaldehyde. Then, they were frozen with OCT compound at −80°C. For immunohistochemical analysis, tissues were sectioned to a thickness of 7 μm. All slices were placed in 0.2% Tween 20 for 10 min, in 3% sodium deoxycholate solution on a shaker for 2–4 h at 37°C, and in 20–50% normal goat serum in 1% bovine serum albumin-PBS solution for 2 h at 37°C. Primary antibody staining was performed using CD68 (1:150; AbD Serotec, Hercules, CA, USA) for macrophage staining and PBR (1:100; Abcam, Cambridge, UK) for TSPO staining at 4°C overnight. Finally, the slices were washed and incubated serially with goat anti-rat IgG antibody (conjugated with Alexa Fluor 488) (1:400; Life Technologies, Carlsbad, CA, USA) for CD68 staining, goat anti-rabbit IgG antibody (Alexa Fluor

647) (1:400; Life Technologies) for PBR staining, Hoechst dye (1:750; Life Technologies) for nuclear staining, and MitoTracker® Orange CM-2TMRos (Life Technologies) for mitochondrial staining. Each stained slide was mounted with Gel-mount solution (Biomeda Corporation, Foster City, CA, USA). Fluorescent images were acquired with an A1 Rsi confocal laser scanning microscope (Nikon, Tokyo, Japan).

Statistical analysis

The uptake of radiotracers and quantification of TSPO expression between groups were compared using IBM SPSS Statistics 19. All data were analyzed by unpaired Student's t-test. Differences with a p-value of less than 0.05 were considered as significant.

2. Fluorescence imaging analysis of tumor models

Fluorescence-labeled and TSPO-targeted nanoparticles

Iron oxide nanoparticles were prepared as previously reported [49]. For stable dispersion and high surface activity, the nanoparticles were surface-treated with polyethyleneglycol (PEG; Samchun Chemical, Seoul, Korea) and polyethylenimine (b-PEI; Sigma, St. Louis, MO, USA). Subsequently, Cy5.5 (Flamma® 675 NHS ester; BioActs, Incheon, Korea), a near-infrared fluorescent dye, was introduced on the surface of the nanoparticles. The primary characteristics of the nanoparticles including size and fluorescence properties were determined (Figure 2). The nanoparticles were observed by transmission electron microscopy (TEM; Carl Zeiss, Oberkochen, Germany) and analyzed by dynamic light scattering (DLS; Malvern Instruments, Malvern, UK), which indicated that the hydrodynamic size of the colloidal nanoparticles was approximately 10 nm in 0.01 M PBS. TSPO-specific ligands (CB235) [50] (Figure 2A) were then added to the nanoparticles, and TSPO-targeted fluorescent nanoparticles were prepared for *in vivo* fluorescence imaging experiments with the tumor models.

Cell lines

U87-MG (human malignant glioblastoma cells), PC-3 (human prostate cancer cells) and U937 (human leukemia cells) were obtained from the

Korean Cell Line Bank (Seoul, Korea). U87-MG was grown in Dulbecco's modified Eagle's medium (DMEM; GE Healthcare, Little Chalfont, UK), and PC-3 and U937 were cultured in Roswell Park Memorial Institute 1640 Medium (RPMI-1640; GE Healthcare) with 10% heat-activated fetal bovine serum (FBS; GE Healthcare) and 1% penicillin-streptomycin (Life Technologies, Carlsbad, CA, USA). The cells were cultured at 37°C in a humidified 5% CO_2 incubator.

Cytotoxicity testing

Cytotoxicity analysis of TSPO-targeted nanoparticles was performed with U937, one of the TSPO-overexpressed cell lines. U937 was seeded in a 24-well plate with 5×10^4 cells per well 24 h before cytotoxicity testing. Then, different concentrations of nanoparticles (15, 30, and 60 μg Fe/mL) were added to each well. The control was not mixed with any nanoparticles (0 μg Fe/mL). After incubation for 2, 4, 8, and 24 h, 20 μL of 0.4% trypan blue solution (Life Technologies, Carlsbad, CA, USA) was added to 20 μL of cell suspension at a 1:1 ratio, and 20 μL of the mixture was transferred to a disposable chamber. The number of viable cells was determined over time using a cell counter (Countess II FL Automated Cell Counter; Life Technologies). The measurement for each condition was repeated three times for accurate comparison.

In vitro cellular uptake analysis

Cells were seeded in a 10 mm cover glass bottom dish (known as a confocal dish) at a density of 5×10^4 cells/dish 24 h before *in vitro* uptake analysis. TSPO-targeted nanoparticles were treated with serum-containing media and added to the cells (20 μg Fe/mL) at 37°C for 4 h. For nuclear and mitochondrial staining, the cells were gently soaked in 1× PBS to avoid detachment. Next, the cells were incubated with Hoechst dye (1:500; Life Technologies, Carlsbad, CA, USA) in serum-free media at 37°C for 20 min followed by 2 μM MitoTracker® Orange CM-H2TMRos (Life Technologies) under the same conditions as for 10 min. These cells were observed with an A1 Rsi confocal laser scanning microscope (Nikon, Tokyo, Japan) at 60× magnification.

Animal models

Male Balb/c athymic mice (6 weeks old) weighing 19–23 g were purchased from Orient Biotech (Seoul, Korea) for *in vivo* assessment. The animals were anesthetized with 2% isoflurane gas, and 5×10^6 U87-MG cells with 100 μL of cold PBS were subcutaneously injected into the forelimb armpit of each mice (n = 15) with a sterile 26-gauge needle. When the tumors reached 0.8–1.0 cm in diameter (after approximately 2 weeks of implantation), the U87-MG xenograft models were used for *in vivo* imaging. All animals were fed a regular diet, and all animal experiments

in this study were performed in accordance with the guidelines of the Institutional Animal Care and Use Committee of Seoul National University (WJIACUC20170123-1-07).

In vivo fluorescence imaging

All animals were anesthetized with 2% isoflurane in oxygen gas, and 200 μg of TSPO-targeted nanoparticles in PBS (100 μL) were injected intravenously into the lateral tail vein using an insulin syringe. *In vivo* fluorescent images were acquired at 30 min, 1 h, 4 h, 8 h, and 24 h post-injection using an *in vivo* imaging system (IVIS Lumina XRMS; Perkin Elmer, Waltham, MA, USA) with the indicated wavelengths (excitation: 660 nm, emission: 710 nm) (Figure 3B). For blocking analysis, fluorescence imaging was performed following the same protocol 10 min after injecting PK11195 (10 mg/kg) to examine the selective displacement of the nanoparticles to TSPO. The mice were kept alive with a body temperature of 37°C during imaging. After noninvasive fluorescence imaging, all mice were euthanized by cervical dislocation. The tumor and major organs were dissected, and fluorescent images were obtained.

Fluorescent image analysis

All images were analyzed by ImageJ (open source image processing software) by calculating the target-to-background ratio (TBR). This value was semi-quantified using a ROI in each fluorescent images of the nanoparticles.

Statistical analysis

The quantification of viable cells in cytotoxicity testing and comparison of the uptake of nanoparticles *in vitro* and *in vivo* were performed using IBM SPSS Statistics 19. All data were analyzed by unpaired Student's t-test. Differences with a p-value of less than 0.05 were considered as significant.

RESULTS AND DISCUSSION

1. Diagnosis of myocarditis by TSPO PET imaging

Radiotracers

The automatic production of two TSPO radiotracers was evaluated using the TRACERlab FX N Pro (for [^{18}F]**1**) and TRACERlab FX$_{FN}$ (for [^{18}F]**2**) module with slight modifications. The results after determining optimal conditions are shown in Table 1. The radiosynthesis of [^{18}F]**1** occurred from $CH_2Br[^{18}F]F$ by *O*-alkylation of desmethyl PBR28 (*N*-acetyl-*N*-(2-hydroxybenzyl)-2-phenoxy-5-pyridinamine) under the automated module system. To perform two separate reactions (aliphatic [^{18}F]fluorination of dibromomethane and *O*-alkylation), we used the TRACERlab FX N Pro module, which is equipped with two reaction vials. By using the optimized procedure, the radiochemical yield was 9.4 ± 3.7% (n = 17, decay corrected) within a synthesis time of 95 ± 1 min, including high-performance liquid chromatography (HPLC) purification. The molar activity of [^{18}F]**1** at the end of the synthesis was 146 ± 39 GBq/μmol. For [^{18}F]**2**, radiosynthesis was performed starting from the tosylate precursor 2-(4-(6,8-dichloro-3-(2-(dipropylamino)-2-oxoethyl)imidazo[1,2- a]pyridine-2-yl)phenoxy)ethyl4-methylbenzenesulfonate through nucleophilic aliphatic substitution. This mixture was extracted by semi-preparative HPLC after approximately 17 min. The radiochemical yield of the final [^{18}F]**2** was 19.7 ± 2.9% (n = 13, non-decay corrected) within a synthesis

time of 70 ± 1 min, including HPLC purification. The molar activity at the end of synthesis was 164 ± 52 GBq/μmol (Table 1).

Metabolite analysis of the heart and plasma

Analysis of the *in vitro* stability of two radiotracers in the human serum demonstrated that the parent peak remained above 99% on the radio-thin-layer chromatography (TLC) profile for 2 h (Table 1). Metabolic stability testing of [^{18}F]**2** in blood and heart homogenates at 60 min after intravenous injection (Figure 4) revealed that [^{18}F]**2** remained stable at 79% in the heart sample, whereas unidentified polar metabolites were found in the blood sample at the same time post-injection. In comparison with metabolites in the blood sample, intact molecules were 13% at 60 min post-injection. The parent peaks were confirmed by co-injection of the cold authentic compound CB251. These results indicated that the generated minor metabolites were the remaining fraction in the blood, suggesting that [^{18}F]**2** is a metabolically stable ligand in the heart that can be used to monitor TSPO overexpression in inflammatory lesions.

PET imaging of the EAM model and control

We evaluated the feasibility of PET imaging using two TSPO radiotracers to noninvasively assess abnormal TSPO expression in the established rat

model of myocarditis (Figure 5). In a comparison study, [^{18}F]**1** revealed no large difference in heart uptake between healthy control and the EAM rats. In contrast, the HLR of [^{18}F]**2** was relatively lower than that of [^{18}F]**1**; however, [^{18}F]**2** showed a significantly higher heart uptake and statistical difference in the HLR between the two groups. Noninvasive *in vivo* assessment of TSPO expression showed a 1.32-fold higher HLR in the inflamed myocardium compared with the healthy myocardium at 60 min post-injection. Furthermore, EAM significantly affected the accumulation of [^{18}F]**2** as shown in the axial microPET image of the heart, and *in vivo* blocking with excess PK11195 resulted in a significantly reduced heart uptake (Figure 6). These results indicated that the myocardium uptake of [^{18}F]**2** in EAM rats was a specific TSPO-mediated immune response against inflammation.

Comparison of TSPO expression in inflamed and healthy heart tissues

We defined the relationship between *in vivo* [^{18}F]**2** accumulation and TSPO expression levels measured by western blotting and immunohistochemistry (Figure 7). TSPO expression levels were approximately 3.7-fold higher in the heart of EAM rats than in that of healthy control rats. Similarly, immunohistochemical results showed that strong fluorescence signals of TSPO were scattered throughout the

inflamed myocardium of EAM rats, and they were concentrated in the macrophages. In comparison with the EAM myocardium, the control myocardium showed minimal TSPO fluorescence. EAM rats displayed extensive inflammatory foci due to macrophage infiltration, whereas healthy control rats showed no inflammatory lesions. The percentage of macrophage expression for EAM versus control rats was 8.79% versus 0.15%, and the percentage of TSPO expression for EAM versus control rats was 20.26% versus 0.90%. Therefore, the high expression of TSPO in the EAM heart tissue can serve as a target for [^{18}F]**2**.

2. Specific visualization of tumors with TSPO-targeted nanoparticles

In vitro toxicity testing

Cellular viability was examined by a trypan blue dye exclusion assay (Figure 8). U937 cells were treated with three different concentrations of TSPO-targeted nanoparticles. More than 80% of the cells survived for 24 h regardless of nanoparticle concentration. Furthermore, we observed that the growth of cells was increased in the presence of the nanoparticles, which may be associated with the induction of the sensitizing activity of monocytes.

In vitro cellular uptake analysis

To demonstrate that the nanoparticles can act as specific ligands for TSPO, the uptake and subcellular localization of TSPO-targeted fluorescent nanoparticles were analyzed following U87-MG or PC-3 incubation (Figure 9). Visualization of nanoparticle uptake by fluorescence microscopy confirmed that the TSPO-targeted nanoparticles were localized in the mitochondria of each cell. Fluorescence microscopy showed that most of the nanoparticles were localized around the mitochondria in the Cy5.5 channel, thus indicating that the nanoparticles were successfully taken up by both U87-MG and PC-3 cells.

Fluorescence imaging

We assessed NIR fluorescence signals in athymic nude mice bearing U87-MG tumors after the intravenous injection of TSPO-targeted fluorescent nanoparticles (Figure 10). All mouse models showed fluorescence immediately after nanoparticle injection. However, the fluorescence in tumors was maintained until 24 h, whereas the surrounding background fluorescence in other tissues or organs was rapidly decreased after 4 h. The fluorescence intensity is defined as photons per second per centimeter squared per steradian (p/s/cm^2/sr) in tumors and other organs. Fluorescence analysis indicated that accumulation in tumors reached a maximum at 8 h post-injection and was slowly washed out over time, demonstrating that the overall nanoparticle uptake in other organs was decreased contrary to the dense deposits in tumors. In the inhibitory experiment, all mice showed fluorescence immediately after injection similar to the non-inhibitory experiments; however, the NIR fluorescence signals in organs and tissues including tumors were successfully reduced after 1 h. Moreover, the *ex vivo* evaluation of excised organs at 8 h and 24 h post-injection showed that the nanoparticles were predominantly taken up by the U87-MG tumor, and the results were significant in terms of fluorescence intensity and contrast. In addition, the TBR was significantly different between the tumor models depending on the presence of PK11195. In particular, the TBR at 24 h post-injection indicated the prolonged and specific uptake of nanoparticles in the tumors.

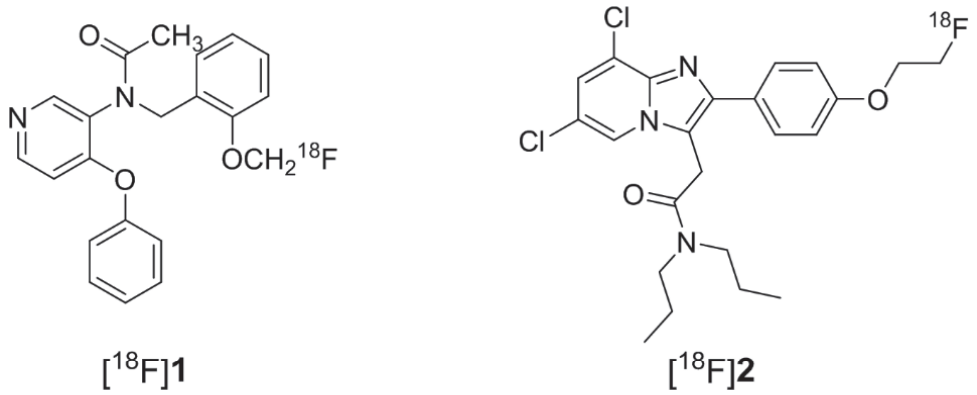

Figure 1. Structure of TSPO imaging radiotracers ([^{18}F]fluoromethyl-PBR28, [^{18}F]**1** and [^{18}F]CB251, [^{18}F]**2**).

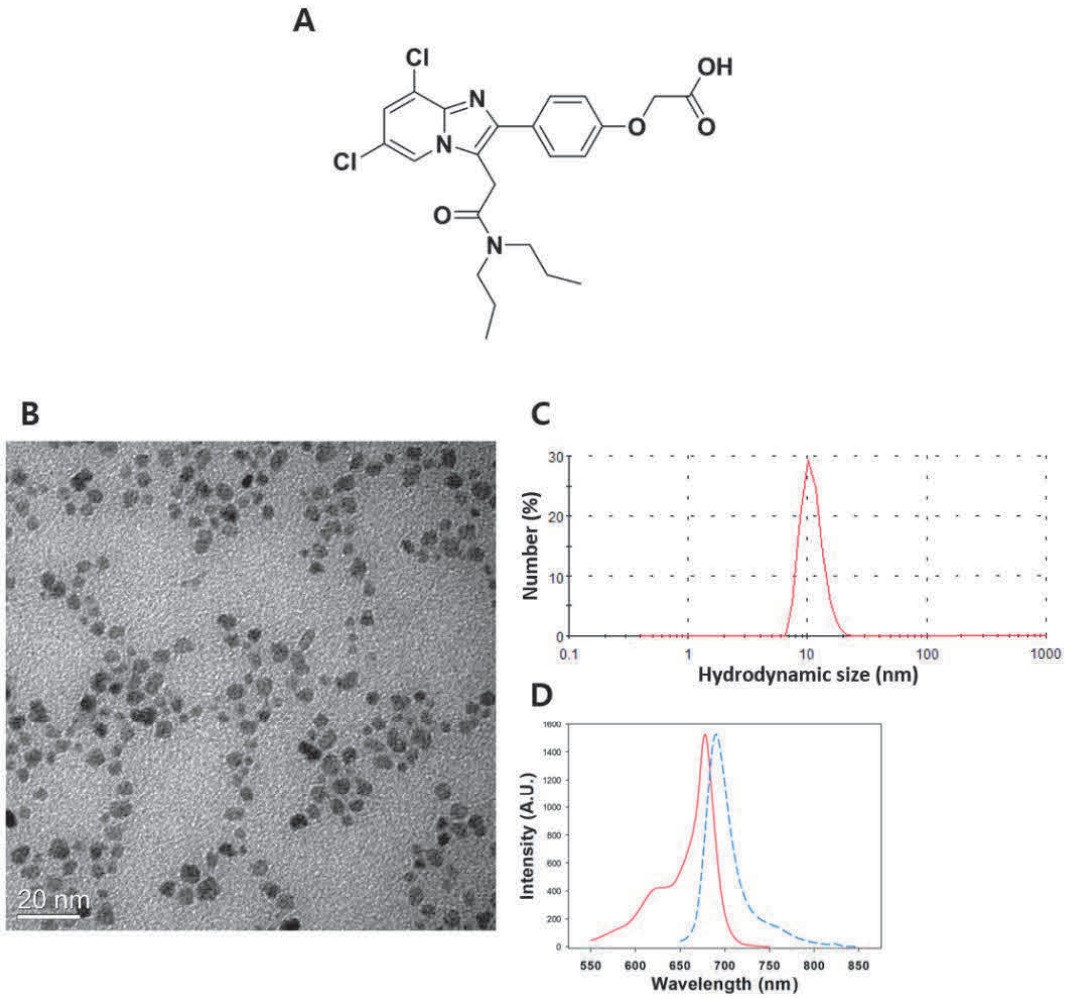

Figure 2. Profiles of TSPO-targeted fluorescent nanoparticles. Structure of TSPO-selective ligand, CB235 (A), representative TEM image (B), hydrodynamic size distribution in 0.01 M PBS (C) of synthesized iron oxide nanoparticles, and fluorescence spectra (red line: excitation, blue dotted line: emission) of Cy5.5 labeled iron oxide nanoparticles (D).

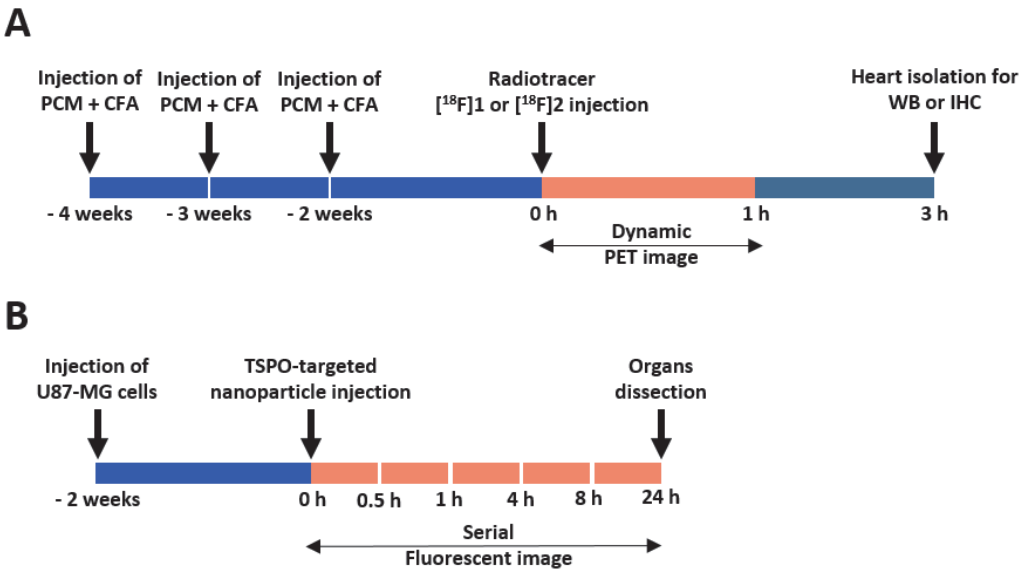

Figure 3. Comprehensive imaging protocol. microPET imaging was performed for 60 min with [^{18}F]fluoromethyl-PBR28 ([^{18}F]**1**) or [^{18}F]CB251 ([^{18}F]**2**) using list-mode (A) and fluorescence images were acquired until 24 h post-injection of nanoparticles (B). PCM; porcine cardiac myosin, CFA; complete Freund's adjuvant, WB; western blot, IHC; immunohistochemistry.

Table 1. Synopsis of two radiotracers, [^{18}F]fluoromethyl-PBR28 ([^{18}F]**1**) and [^{18}F]CB251 ([^{18}F]**2**).

	[^{18}F]**1**	[^{18}F]**2**
Used synthetic module	TRACERlab FX N Pro	TRACERlab FX_{FN}
Radiochemical yield (%)[a]	9.4 ± 3.7	19.7 ± 2.9
Radiochemical purity (%)	> 99	> 98
Molar activity (GBq/μmol)	146 ± 39	164 ± 52
Total synthetic time (min)	95 ± 1	70 ± 1
In vitro stability in human serum (%, 2 h)	> 99	> 99

[a] Data reported are decay corrected at EOS and represent the mean and standard deviations of over five experiments.

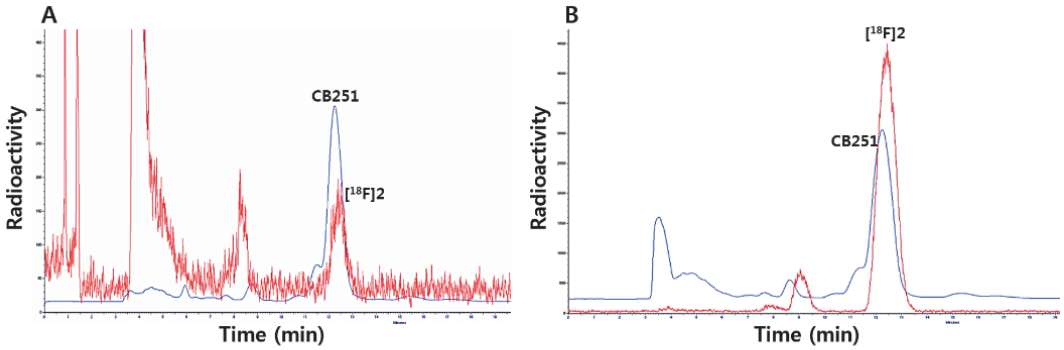

Figure 4. Identification of parent and metabolites of [^{18}F]CB251 ([^{18}F]**2**) in normal mice. HPLC profiles of each samples with an authentic compound CB251 (Red: gamma-ray, Blue: UV-254 nm); blood samples (A) and heart samples (B) at 60 min post-injection.

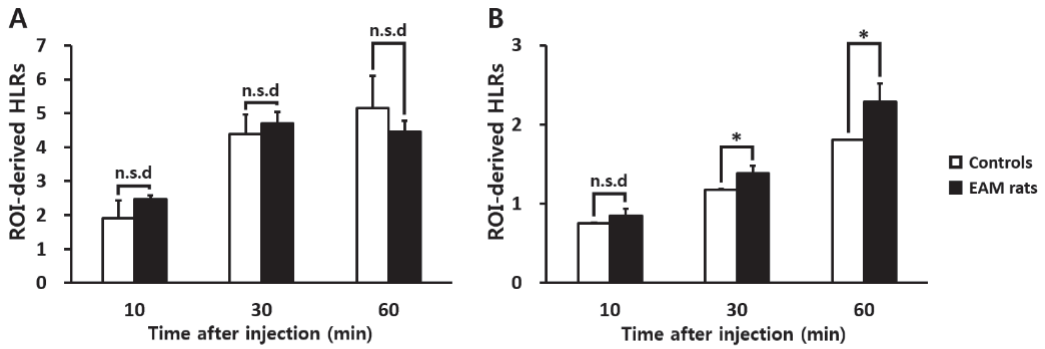

Figure 5. Comparison of ROI-derived heart-to-lung ratios (HLRs) of [^{18}F]fluoromethyl-PBR28 ([^{18}F]**1**) (A) and [^{18}F]CB251 ([^{18}F]**2**) (B) depending on the *in vivo* incubation time between the controls and EAM rats. (*$p < 0.05$). n.s.d; no significant difference.

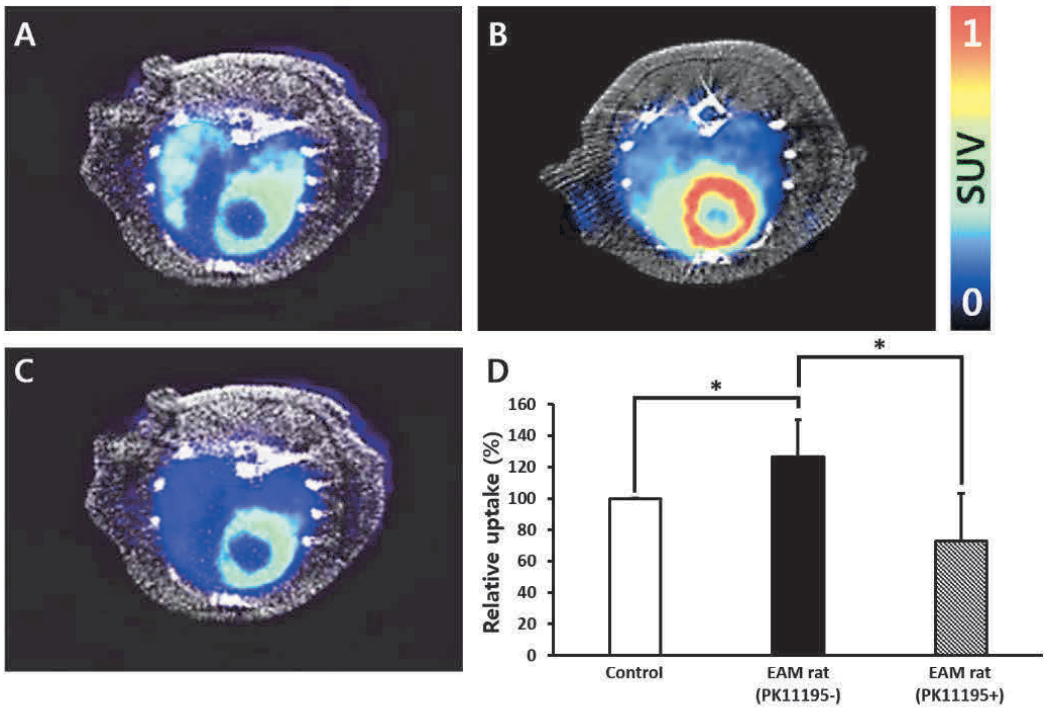

Figure 6. Representative microPET axial heart images and comparison of relative uptake value of [^{18}F]CB251 ([^{18}F]**2**) in the control and EAM rat at 60 min post-injection. PET images of the heart in the healthy control (A), EAM rat (B), and EAM rat after PK11195 pre-treatment (C). Relative uptake in these three groups at 60 min post-injection of [^{18}F]**2** (*$p < 0.05$) (D). The relative uptake level of [^{18}F]**2** expressed as heart uptake in EAM rat depending on presence of PK11195 compared to that of a healthy control.

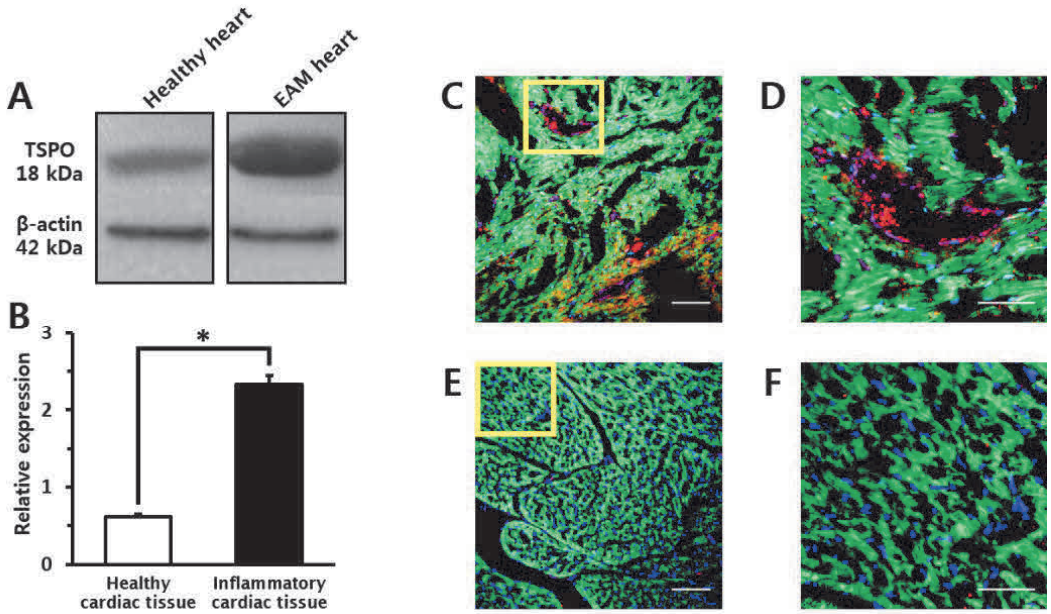

Figure 7. *Ex vivo* analysis of TSPO expression. Western blotting analysis of heart samples (A, B). (*$p < 0.01$). Representative immunohistochemical images indicating the expression level of CD68+ macrophages and TSPO in inflammatory myocardial tissue (C, D) and healthy myocardial tissue (E, F) by confocal laser scanning microscopy. Highly magnified images of the yellow rectangle in C and E respectively (D, F). Blue: nucleus, green: mitochondria, red: TSPO, magenta: macrophage. Scale bars, 100 μm (20×) & 50 μm (60×).

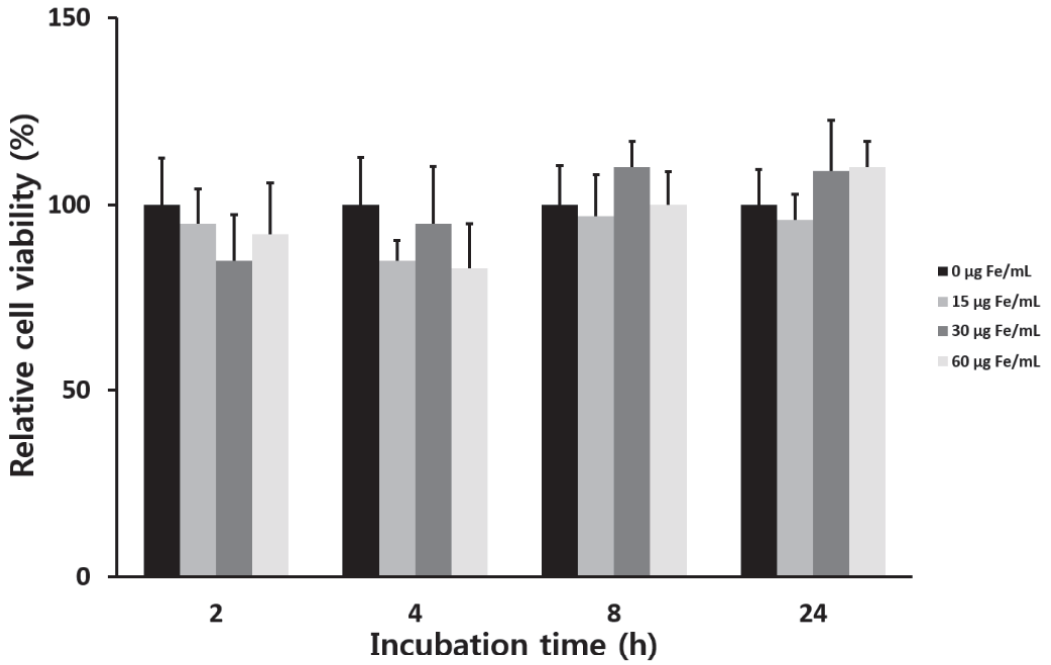

Figure 8. Cytotoxicity testing of nanoparticles assessed by trypan blue exclusion. Nanoparticles of 0 µg Fe/mL (black bar) as control, 15 µg Fe/mL (grey bar), 30 µg Fe/mL (dark grey bar), and 60 µg Fe/mL (light grey bar) were incubated into U937 cells for 2 h, 4 h, 8 h, and 24 h respectively. The relative cell viability depending on different nanoparticle concentrations and incubation times did not show any significant statistical difference.

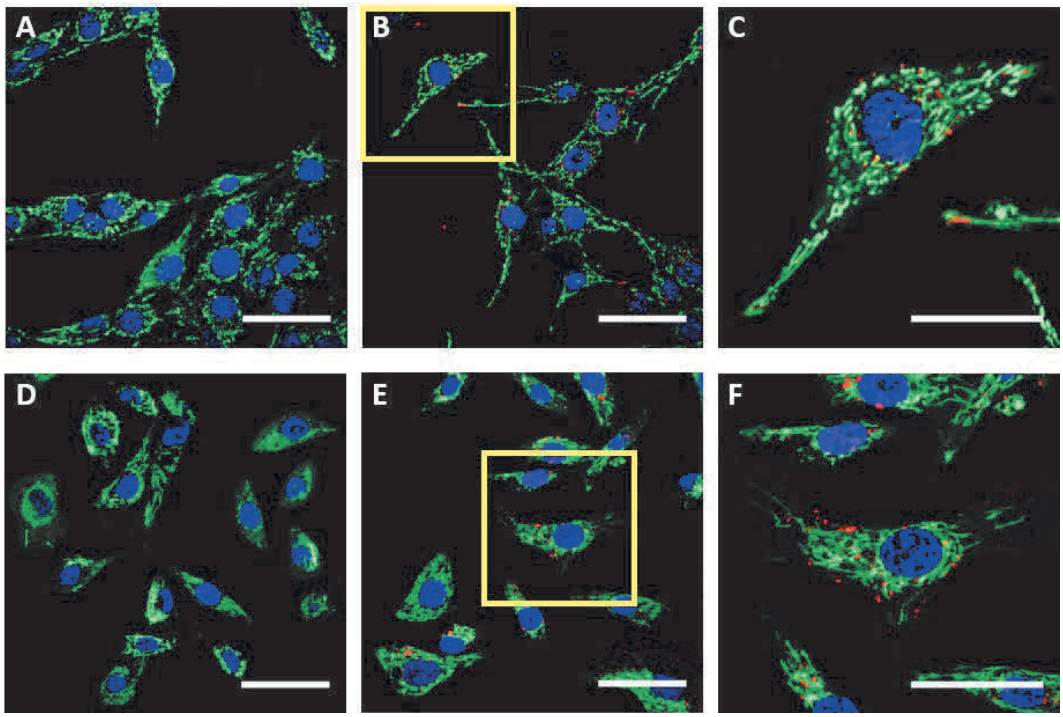

Figure 9. *In vitro* uptake analysis of nanoparticles in U87-MG (A-C) and PC-3 (D-F). TSPO-targeted nanoparticles of 0 μg Fe/mL (A,D) as control and 20 μg Fe/mL (B,E) were treated into each cells and incubated for 4 h. Each single cell was observed with high magnified fluorescent images of the yellow rectangle in B and E respectively (C,F). Blue: nucleus, green: mitochondria, red: nanoparticles. Scale bars, 10 μm (60×) & 5 μm (180×).

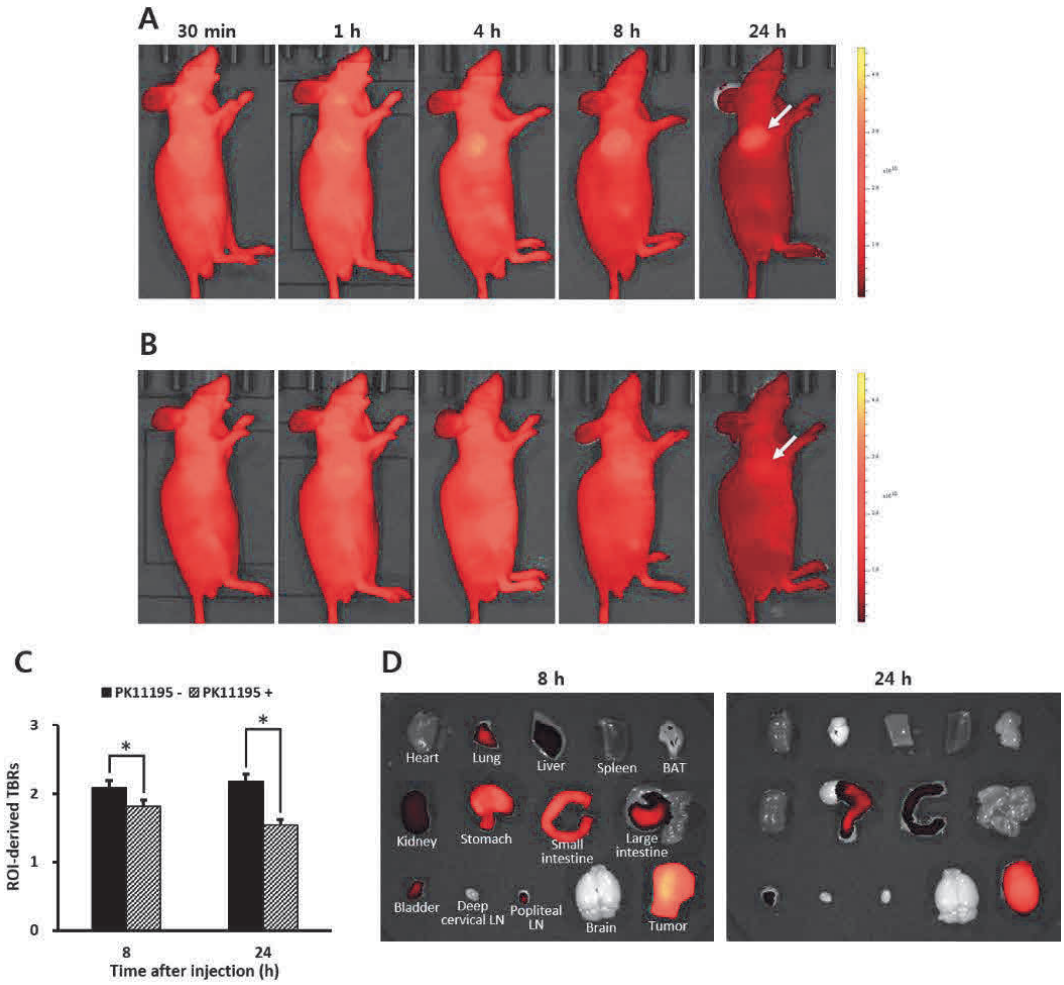

Figure 10. Comparison of fluorescence images and tumor uptake of nanoparticles. *In vivo* fluorescence imaging was performed at 30 min, 1 h, 4 h, 8 h, and 24 h post-injection of TSPO-targeted nanoparticles (A). The blocking study with PK11195 pre-treatment was proceeded through same imaging protocol above mentioned (B). ROI-derived tumor-to-background ratios (TBRs) of the nanoparticles in mouse models at 8 h and 24 h post-injection depending on the presence of PK11195 was analyzed (*$p < 0.05$) (C). *Ex vivo* fluorescent images were acquired at 8 h and 24 h after sacrificing each mice (D).

CONCLUSION

In this study, we revealed that the *in vivo* potency of radiotracers distributed in the inflammatory myocardial regions of rats is critically dependent on their binding affinity to TSPO. Furthermore, the chemical structural differences between the two classes of radiotracers may affect the visualization of TSPO expression in inflammatory lesions. As expected, based on our previous *in vitro* TSPO-binding study, the HLR of [^{18}F]**2** in EAM rats was 1.32-fold higher than of that in healthy control rats. Comparably, TSPO expression was 3.7-fold higher in inflammatory heart tissues than in healthy heart tissues as indicated by western blotting. However, [^{18}F]**1** did not show a significant difference in the HLR between the two groups. The findings indicated that [^{18}F]**2** would be a more suitable radiotracer than [^{18}F]**1** for detecting inflammatory myocardial foci considering its higher TSPO-binding affinity. Moreover, fluorescence imaging of the glioblastoma xenograft mouse model revealed the high accumulation of TSPO-targeted nanoparticles in tumors. In comparison with mouse groups pre-treated with PK11195, mouse groups without PK11195 showed specific and prolonged uptake in tumors despite rapid clearance in other organs. Nanoparticle accumulation was the highest at 8 h, and 71.3% of the uptake at 8 h was maintained for 24 h after injection. The uptake pattern was considerably different depending on the presence of PK11195, suggesting that nanoparticles prepared with CB235, a TSPO-selective ligand, are suitable for

the specific visualization of glioblastoma because of the high selectivity for TSPO.

In summary, we successfully demonstrated the feasibility of using TSPO radiotracers ([^{18}F]**2**) with PET imaging to specifically detect EAM and of using TSPO-targeted fluorescent nanoparticles with optical imaging to visualize tumors in the preclinical stage. It is beyond the scope of this research to determine whether the radiotracers and nanoparticles can be used for clinical purposes. However, we believe that early-stage human myocarditis or brain cancer can be diagnosed using [^{18}F]**2** or fluorescent imaging probes in the future.

REFERENCES

1. Papadopoulos V, Baraldi M, Guilarte TR, Knudsen TB, Lacapère JJ, Lindemann P, Norenberg MD, Nutt D, Weizman A, Zhang MR, Gavish M. Translocator protein (18 kDa): new nomenclature for the peripheral-type benzodiazepine receptor based on its structure and molecular function. *Trends. Pharmacol. Sci*. 2006;**27**:402-409.
2. Rupprecht R, Papadopoulos V, Rammes G, Baghai TC, Fan J, Akula N, Groyer G, Adams D, Schumacher M. Translocator protein (18 kDa) (TSPO) as a therapeutic target for neurological and psychiatric disorders. *Nat Rev Drug Discov*. 2010;**9**:971-988.
3. Liu GJ, Middleton RJ, Hatty CR, Kam WW, Chan R, Pham T, Harrison-Brown M, Dodson E, Veale K, Banati RB. The 18 kDa translocator protein, microglia and neuroinflammation. *Brain Pathol*. 2014;**24**:631-653.
4. Gavish M, Bachman I, Shoukrun R, Katz Y, Veenman L, Weisinger G, Weizman A. Enigma of the peripheral benzodiazepine receptor. *Pharmacol Rev*. 1999;**51**:629-650.
5. Casellas P, Galiegue S, Basile AS. Peripheral benzodiazepine receptors and mitochondrial function. *Neurochem Int*. 2002;**40**:475-486.
6. Veenman L, Papadopoulos V, Gavish M. Channel-like functions of the 18-kDa translocator protein (TSPO): regulation of apoptosis and steroidogenesis as part of the host-defense response. *Curr Pharm Des*. 2007;**13**:2385-2405.
7. Cosenza-Nashat M, Zhao ML, Suh HS, Morgan J, Natividad R, Morgello S, Lee SC. Expression of the translocator protein of 18 kDa by microglia, macrophages and astrocytes based on immunohistochemical localization in abnormal human brain. *Neuropathol Appl Neurobiol*. 2009;**35**:306-328.
8. Han Z, Slack RS, Li W, Papadopoulos V. Expression of peripheral benzodiazepine receptor (PBR) in human tumors: relationship to breast, colorectal, and prostate tumor progression. *J Recept Signal Transduct Res*. 2003;**23**:225-238.
9. Kim T, Pae AN. Translocator protein (TSPO) ligands for the diagnosis or treatment of neurodegenerative diseases: a patent review (2010 - 2015; part 2). *Expert Opin Ther Pat*. 2016;**26**:1353-1366.
10. Qi X, Xu J, Wang F, Xiao J. Translocator protein (18 kDa): a promising therapeutic target and diagnostic tool for cardiovascular diseases. *Oxid Med Cell Longev*. 2012;**2012**:162934.
11. Austin CJ, Kahlert J, Kassiou M, Rendina LM. The translocator protein (TSPO): a novel target for cancer chemotherapy. *Int J Biochem Cell Biol*. 2013;**45**:1212-1216.
12. Omami G, Tamimi D, Branstetter BF. Basic principles and applications of (18)F-FDG-PET/CT in oral and maxillofacial imaging: A pictorial essay. *Imaging Sci Dent*. 2014;**44**:325-332.

13. Laissy JP, Hyafil F, Feldman LJ, Juliard JM, Schouman-Claeys E, Steg PG, Faraggi M. Differentiating acute myocardial infarction from myocarditis: diagnostic value of early- and delayed-perfusion cardiac MR imaging. *Radiology*. 2005;**237**:75-82.
14. Angelini A, Calzolari V, Calabrese F, Boffa G, Maddalena F, Chioin R, Thiene G. Myocarditis mimicking acute myocardial infarction: role of endomyocardial biopsy in the differential diagnosis. *Heart*. 2000;**84**:245-250.
15. Kindermann I, Barth C, Mahfoud F, Ukena C, Lenski M, Yilmaz A, Klingel K, Kandolf R, Sechtem U, Cooper LT, Böhm M. Update on myocarditis. *J Am Coll Cardiol*. **2012**, *59*, 779-792.
16. Dancea AB. Myocarditis in infants and children: A review for the paediatrician. *Paediatr Child Health*. 2001;**6**:543-545.
17. Matsuura H, Ichida F, Saji T, Ogawa S, Waki K, Kaneko M, Tahara M, Soga T, Ono Y, Yasukochi S. Clinical Features of Acute and Fulminant Myocarditis in Children - 2nd Nationwide Survey by Japanese Society of Pediatric Cardiology and Cardiac Surgery. *Circ J*. 2016;**80**:2362-2368.
18. Fabre A, Sheppard MN. Sudden adult death syndrome and other non-ischaemic causes of sudden cardiac death. *Heart*. 2006;**92**:316-320.
19. Aretz, HT, Billingham ME, Edwards WD, Factor SM, Fallon JT, Fenoglio JJ.Jr, Olsen EG, Schoen FJ. Myocarditis. A histopathologic definition and classification. *Am J Cardiovasc Pathol*. 1987;**1**: 3-14.
20. Cooper LT, Baughman KL, Feldman AM, Frustaci A, Jessup M, Kuhl U, Levine GN, Narula J, Starling RC, Towbin J, Virmani R. The role of endomyocardial biopsy in the management of cardiovascular disease: a scientific statement from the American Heart Association, the American College of Cardiology, and the European Society of Cardiology. Endorsed by the Heart Failure Society of America and the Heart Failure Association of the European Society of Cardiology. *Eur Heart J*. 2007;**28**:3076-3093.
21. Skouri HN, Dec GW, Friedrich MG, Cooper LT. Noninvasive imaging in myocarditis. *J Am Coll Cardiol*. 2006;**48**:2085-2093.
22. Parsai C, O'Hanlon R, Prasad SK, Mohiaddin RH. Diagnostic and prognostic value of cardiovascular magnetic resonance in non-ischaemic cardiomyopathies. *J Cardiovasc Magn Reson*. 2012;**14**:54.
23. James OG, Christensen JD, Wong TZ, Borges-Neto S, Koweek LM. Utility of FDG PET/CT in inflammatory cardiovascular disease. *Radiographics*. 2011;**31**:1271-1286.
24. Kircher M, Lapa C. Novel Noninvasive Nuclear Medicine Imaging Techniques for Cardiac Inflammation. *Curr Cardiovasc Imaging Rep*. 2017;**10**:6.
25. Moon BS, Kim BS, Park C, Jung JH, Lee YW, Lee HY, Chi DY, Lee BC, Kim SE. [^{18}F]Fluoromethyl-PBR28 as a potential radiotracer for TSPO: preclinical comparison with [^{11}C]PBR28 in a rat model of neuroinflammation. *Bioconjug Chem*. 2014;**25**:442-450.
26. Perrone M, Moon BS, Park HS, Laquintana V, Jung JH, Cutrignelli A, Lopedota A, Franco M, Kim SE, Lee BC, Denora N. A Novel PET

Imaging Probe for the Detection and Monitoring of Translocator Protein 18 kDa Expression in Pathological Disorders. *Sci Rep*. 2016;**6**:20422.
27. Wang H, Pullambhatla M, Guilarte TR, Mease RC, Pomper MG. Synthesis of [^{125}I]IodoDPA-713, a new probe for imaging inflammation. *Biochem Biophys Res Commun*. 2009;**389**:80-83.
28. Fairweather D, Coronado MJ, Garton AE, Dziedzic JL, Bucek A, Cooper LT Jr, Brandt JE, Alikhan FS, Wang H, Endres CJ, Choi J, Pomper MG, Guilarte TR. Sex differences in translocator protein 18 kDa (TSPO) in the heart: implications for imaging myocardial inflammation. *J Cardiovasc Transl Res*. 2014;**7**:192-202.
29. Hanif F, Muzaffar K, Perveen K, Malhi SM, Simjee ShU. Glioblastoma Multiforme: A Review of its Epidemiology and Pathogenesis through Clinical Presentation and Treatment. *Asian Pac J Cancer Prev*. 2017;**18**:3-9.
30. Parsons DW, Jones S, Zhang X, Lin JC, Leary RJ, Angenendt P, Mankoo P, Carter H, Siu IM, Gallia GL, Olivi A, McLendon R, Rasheed BA, Keir S, Nikolskaya T, Nikolsky Y, Busam DA, Tekleab H, Diaz LA Jr, Hartigan J, Smith DR, Strausberg RL, Marie SK, Shinjo SM, Yan H, Riggins GJ, Bigner DD, Karchin R, Papadopoulos N, Parmigiani G, Vogelstein B, Velculescu VE, Kinzler KW. An integrated genomic analysis of human glioblastoma multiforme. *Science*. 2008;**321**:1807-1812.
31. Batash R, Asna N, Schaffer P, Francis N, Schaffer M. Glioblastoma Multiforme, Diagnosis and Treatment; Recent Literature Review. *Curr Med Chem*. 2017;**24**:3002-3009.
32. Lieberman F. Glioblastoma update: molecular biology, diagnosis, treatment, response assessment, and translational clinical trials. *F1000Research*. 2017;**6**:1892.
33. Fink JR, Muzi M, Peck M, Krohn KA. Continuing Education: Multi-modality Brain Tumor Imaging – MRI, PET, and PET/MRI. *J Nucl Med*. 2015;**56**:1554-1561.
34. la Fougère C, Suchorska B, Bartenstein P, Kreth FW, Tonn JC. Molecular imaging of gliomas with PET: opportunities and limitations. *Neuro Oncol*. 2011;**13**:806-819.
35. Spalding K, Board R, Dawson T, Jenkinson MD, Baker MJ. A review of novel analytical diagnostics for liquid biopsies: spectroscopic and spectrometric serum profiling of primary and secondary brain tumors. *Brain Behav*. 2016;**6**:e00502.
36. Piccirillo SG, Dietz S, Madhu B, Griffiths J, Price SJ, Collins VP, Watts C. Fluorescence-guided surgical sampling of glioblastoma identifies phenotypically distinct tumour-initiating cell populations in the tumour mass and margin. *Br J Cancer*. 2012;**107**:462-468.
37. Price SJ, Gillard JH. Imaging biomarkers of brain tumour margin and tumour invasion. *Br J Cancer*. 2011;**84**:S159-167.
38. Landau MJ, Gould DJ, Patel KM. Advances in fluorescent-image guided surgery. *Ann Transl Med*. 2016;**4**:392.

39. Mondal SB, Gao S, Zhu N, Liang R, Gruev V, Achilefu S. Real-time fluorescence image-guided oncologic surgery. *Adv Cancer Res*. 2014;**124**:171-211.
40. Hong G, Antaris AL, Dai H. Near-infrared fluorophores for biomedical imaging. *Nat Biomed Eng*. 2017;**1**:0044.
41. Bonis-O'Donnell JTD, Page RH, Beyene AG, Tindall EG, McFarlane IR, Landry MP. Dual Near-Infrared Two-Photon Microscopy for Deep-Tissue Dopamine Nanosensor Imaging. *Adv Funct Mater*. 2017;**27**:1702112.
42. Zanganeh S, Hutter G, Spitler R, Lenkov O, Mahmoudi M, Shaw A, Pajarinen JS, Nejadnik H, Goodman S, Moseley M, Coussens LM, Daldrup-Link HE. Iron oxide nanoparticles inhibit tumour growth by inducing pro-inflammatory macrophage polarization in tumour tissues. *Nat Nanotechnol*. 2016;**11**:986-994.
43. Minchin RF, Martin DJ. Minireview: Nanoparticles for Molecular Imaging—An Overview. *Endocrinology*. 2010;**151**:474-481.
44. Ali A, Zafar H, Zia M, Ul Haq I, Phull AR, Ali JS, Hussain A. Synthesis, characterization, applications, and challenges of iron oxide nanoparticles. *Nanotechnol Sci Appl*. 2016;**9**: 49-67.
45. Denora N, Laquintana V, Pisu MG, Dore R, Murru L, Latrofa A, Trapani G, Sanna E. 2-Phenyl-imidazo[1,2-a]pyridine compounds containing hydrophilic groups as potent and selective ligands for peripheral benzodiazepine receptors: synthesis, binding affinity and electrophysiological studies. *J Med Chem*. 2008;**51**:6876-6888.
46. Schmerler P, Jeuthe S, O h-Ici D, Wassilew K, Lauer D, Kaschina E, Kintscher U, Müller S, Muench F, Kuehne T, Berger F, Unger T, Steckelings UM, Paulis L, Messroghli D. Mortality and morbidity in different immunization protocols for experimental autoimmune myocarditis in rats. *Acta Physiol (Oxf)*. 2014;**210**:889-898.
47. Huisman MC, Higuchi T, Reder S, Nekolla SG, Poethko T, Wester HJ, Ziegler SI, Casebier DS, Robinson SP, Schwaiger M. Initial characterization of an 18F-labeled myocardial perfusion tracer. *J Nucl Med*. 2008;**49**:630-636.
48. Mahmood T, Yang PC. Western blot: technique, theory, and trouble shooting. *N Am J Med Sci*. 2012;**4**:429-434.
49. Yang KM, Cho HI, Choi HJ, Piao Y. Synthesis of water well-dispersed PEGylated iron oxide nanoparticles for MR/optical lymph node imaging. *J Mater Chem B*. 2014;**2**:3355-3364.
50. Denora N, Laquintana V, Lopalco A, Iacobazzi RM, Lopedota A, Cutrignelli A, Iacobellis G, Annese C, Cascione M, Leporatti S, Franco M. In vitro targeting and imaging the translocator protein TSPO 18-kDa through G(4)-PAMAM-FITC labeled dendrimer. *J Control Release*. 2013;**172**:1111-1125.

국문초록

심근염 및 교모세포종 모델에서 PET과 형광영상을 이용한 전이체 단백질 18 kDa 발현의 평가

전이체 단백질 (Translocator protein 18 kDa, TSPO)은 미토콘드리아 외막에 위치하는 단백질로서 염증부위와 특정 종양에서 과 발현되는 특성에 의해 질병 진단을 위한 중요한 바이오마커로 알려져 있다. TSPO의 과 발현은 질환에서의 염증반응과 밀접한 관련이 있으며, 심근염과 다형성교모세포종 역시도 이에 해당한다. 본 연구에서는 랫드 자가면역 심근염 모델과 교모세포종 누드 마우스 모델에서 각각 [^{18}F]fluoromethyl-PBR28 ([^{18}F]**1**)과 [^{18}F]CB251 ([^{18}F]**2**)의 방사성추적자와 TSPO 표적 산화철 나노입자를 이용하여 TSPO 발현을 평가하였다. [^{18}F]**1**과 [^{18}F]**2**는 자동합성장치를 이용한 합성방식으로 준비하였고, 양전자방출단층촬영 (PET)을 통해 랫드 자가면역 심근염 모델과 대조군 사이에서 심근 염증 부위에 대한 특이적 TSPO 발현을 추적 및 비교하였다. [^{18}F]**2**는 주입 60분 후 심근염 모델의 병소에서 특이적이고 높은 TSPO 섭취를 보였고, 섭취율에 대한 심폐계수에서도 대조군에 비해 1.32배 높은 수치를 보였다. 반면에, [^{18}F]**1**은 심근염 모델과 대조군 사이에서 유

의미한 차이를 보이지 않았다. 각각의 그룹에서 적출한 심장에서의 조직학적 분석은 염증이 발생한 심근에서의 TSPO 과 발현율을 제시하였다. 산화철 나노입자는 TSPO 표적 리간드와 Cy5.5 염료가 표면에 부착된 형태로 제작되었고, 마우스 종양 모델에서의 형광영상으로 TSPO 발현을 평가하였다. 종양 모델에서의 생체 내 섭취 양상은 나노입자 주입 후 8시간 째 가장 강한 형광신호가 종양에서 획득되었고, 다른 기관에서의 빠른 대사에도 불구하고 24시간까지 약 71.3%의 형광신호가 종양에서 유지됨을 확인하였다. 종양 대 배경 신호비도 24시간에서 가장 높게 나타났다. 이번 연구에서는 이미다조피리딘 아세트아마이드 계 물질인 [^{18}F]**2**가 과 발현된 TSPO를 표적하여 염증을 진단케 하는 비침습성 진단용 방사성추적자로서 높은 민감성을 보였음이 확인되었다. 따라서, 임상적 적용 조건을 갖춘 [^{18}F]**2** PET영상으로 하여금 심근염 환자의 효과적인 진단이 가능할 것으로 기대된다. 또한, TSPO 표적 나노입자는 특이적인 종양 영상화의 가능성을 확인하였다. 이를 토대로, 높은 표적성과 선택성을 지니는 TSPO 표적 나노입자를 이용하여 종양 절제술용 가이드 형광영상으로 그 활용성을 확장하고자 한다.

중심단어: 전이체 단백질, 심근염, 다형성교모세포종, 양전자방출단층촬영, 형광영상

학번: 2016-26046